

Self-rotation in electrocapillary flows

M. A. Herrada and A. Barrero

Escuela Superior de Ingenieros, Universidad de Sevilla, Camino de los Descubrimientos s/n, 41092 Sevilla, Spain

(Received 2 April 2002; published 24 September 2002)

The mechanism of appearance of swirl in a certain class of converging flows is investigated numerically. The analysis is motivated by the spontaneous generation of swirl, which has been observed in electrified menisci (Taylor cones). The electrical stress acting on the cone surface drives these electrified millimetric fluid flows. Numerical results show that the primarily swirl-free meridian flow is unstable within an interval of values of the Reynolds number based on the surface stress. For values of the Reynolds number outside this interval, which depends on the forcing conditions and the geometry of the flow, the nonswirling meridian flow is stable. The instability mechanism of circulation amplification, which has nothing to do with the well-known increase of swirl velocity due to the vortex stretching mechanism, is due to a convection-diffusion effect. The circulation accumulated at the axis zone by the converging meridian motion is pumped by diffusion toward the conical surface. This feedback loop mechanism shoots the circulation amplification for values of the Reynolds number larger than a critical one. The same instability mechanism of swirl amplification could also appear in other converging flows generated by body forces (natural convection, electrical forces, etc.).

DOI: 10.1103/PhysRevE.66.036311

PACS number(s): 47.20.-k, 47.32.-y, 47.65.+a

I. INTRODUCTION

Swirl generation in fluid masses without any apparent cause leading to it, namely self-rotation, is met in many natural systems. For example, the rotation observed in spiral galaxies, protostar nebulae, and other astrophysical objects [1]. Hurricanes and tornadoes are also examples of natural flows where the generation of circulation remains also unexplained. In a more humble scenario, the bathtub vortex is a classical example closely related to self-rotation [2]. A careful experimental investigation on swirl generation in a bathtub, [3] has shown that swirling motion around the sinkhole appears only when the sink flow rate exceeds some threshold value. In any case, whether the bathtub vortex is either due to symmetry breaking at a certain threshold value of some parameter of the problem or external forcing is still a matter of controversy [4]. A recent experimental investigation on the appearance of swirl in a confined sink flow [5] suggests that the formation of the vortex is due to a supercritical bifurcation at a certain critical Reynolds number. In addition to the above mentioned cases, other examples of spontaneous appearance of circulation in flows under well-controlled experimental conditions are, i.e., free convection in a sealed cylinder [6]; a horizontally oscillating glass of water [7]; an electrically driven flow of mercury in a cup [8]; and the flow inside electrified menisci [9] (Taylor cones in the electro-spray literature).

Although spontaneous circulation is a common feature in all these different flows, the physical mechanism leading to it can be entirely different for each one of them. Here, we are interested in the discussion of the mechanism of spontaneous appearance circulation (swirl) in primarily swirl-free, meridian recirculatory flows. Note that we refer to generation of circulation instead of generation of large swirl velocities with constant circulation as it occurs, for instance, in converging flows due to the vortex stretching mechanism (angular conservation momentum). Meridian recirculatory flows take place inside electrified menisci (Taylor cones), or in the Bo-

jarevics experiment among others. A Taylor cone forms at the exit of an electrified needle when a liquid is injected through it at appropriate flow rates. Details of a typical experimental setup are given in Ref. [10] among many others [11].

Liquid motions inside the Taylor cone, which have been recently investigated, in Refs. [9] and [12], are driven by both the tangential component of the electrical stress acting on the gas-liquid interface of the meniscus and the injected value of the flow rate. Moreover, as shown by experiments, the flow pattern depends strongly on the properties of the liquid that is being electrosprayed, mainly the viscosity μ and the electrical conductivity K . In fact, when liquids with sufficiently high values of both electrical conductivity and viscosity are electrosprayed no noticeable motion different from the pure sink flow corresponding to the imposed value of the flow rate Q is observed. For such liquids the voltage drop in the liquid is so small that the tangential electrical stress on the surface is negligible.

When we use liquids with smaller values of the electrical conductivity and viscosity, the tangential electrical stress at the surface increases and, consequently, the velocity induced by the stress increases too. If this characteristic velocity is larger than that due to the flow rate, a recirculating meridian motion, towards the apex along the generatrix and away from it along the axis, appears. The liquid lying close to the surface is ejected through the jet while the rest recirculates towards the apex along the generatrix. The two flows are separated by a dividing stream surface passing through a stagnation point located at the axis at a certain distance from the cone vertex. Figure 1 shows the projections of the particle path lines on the meridian plane of a Taylor cone orthogonal to the observation axis. It should be pointed out that the shape of the electrified meniscus becomes more conical as the applied voltage increases, but the flow pattern remains essentially identical to the one in Fig. 1. Propylene glycol doped with a small amount of hydrochloric acid to enhance its electrical conductivity ($K=0.015$ S/m) has been used.

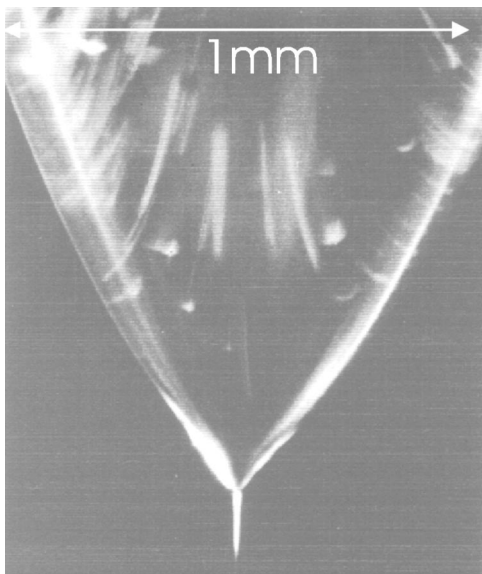


FIG. 1. Particle path lines in an electrified meniscus of propylene glycol. No azimuthal velocities are observed in this case.

Also, similar flow patterns are observed when other liquids with values of both the viscosity and the electrical conductivity of the same order are used.

In contrast, it is found that the streamlines are not contained in meridian planes when liquids with sufficiently small values of both the electrical conductivity and the viscosity are electrospayed (the case of liquid paraffins and some alcohols), see Fig. 2. As shown in the figure, there are an intense motion in the azimuthal direction (swirl) in addition to the meridian one. Figure 2, which results from superposition of several consecutive video frames, shows the projections of the particle path lines on the meridian plane of the Taylor cone orthogonal to the observation axis. Ethanol, as purchased, which has values of the conductivity and viscos-

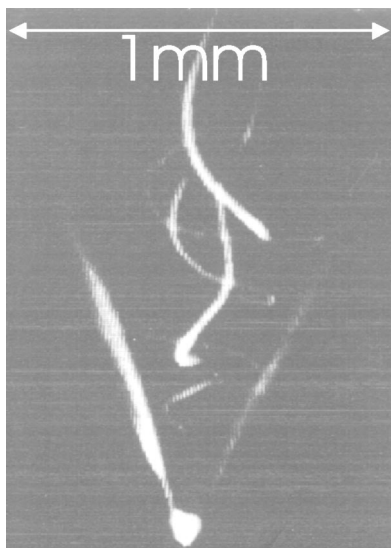


FIG. 2. Particle path lines in an electrified meniscus of ethanol. Trajectories show unambiguously the existence of an intense swirl in the liquid motion.

ity much smaller than those of the propylene glycol (~ 1500 and 60 times less conducting and viscous) was the liquid used in this experiment.

The Reynolds number, defined from a characteristic velocity of the liquid and the needle diameter is the only dynamical parameter making a difference between the two cases considered in Figs. 1 and 2. Based on experimental observations, the Reynolds number of the motion was estimated to be 3×10^{-3} for the propylene glycol case and 50 for the ethanol case [9,12].

To explain the appearance of circulation in primarily meridian recirculatory flows such as the ones inside Taylor cones [12] (also in the experiment by Bojarevics [8,13]) we considered the self-similar motion of a liquid inside an unbounded cone driven by a stress in the radial direction, which varies as the inverse of the square distance to the cone vertex r^* ; the component of the stress in the azimuthal direction being zero. Thus, the Navier-Stokes equations reduce to a system of nonlinear ordinary differential equations that determines the velocity vector and pressure field. The results of the self-similar analysis show that swirl appears owing to bifurcation from a primarily swirl-less meridian flow where the liquid moves towards the vertex along the generatrix and away from it along the axis. This bifurcation occurs when a characteristic Reynolds number of the motion is larger than a threshold value.

Clearly, the assumption of an unbounded conical domain required for the existence of self-similar solutions could put some restrictions for the relevance of the self-similar results regarding to real flows inside Taylor cones. Another drawback of the analysis by Shtern and Barrero [12] is that, in real Taylor cones, the tangential component of the electrical stress scales with the distance to the vertex in the form $r^{*-2.5}$, see Ref. [10], while an r^{*-2} dependence is required for the Navier-Stokes equations becomes self-similar. It should be pointed out that for very high Reynolds numbers, the Euler equations also admit self-similar conical solutions if the driving stress has the form $\tau_{r^*,\theta} \sim r^{*-l}$ (l being any real number) [14]. Nonetheless, such inviscid analysis is not appropriate to investigate the existence of bifurcations at finite values of the Reynolds number.

To enhance the knowledge on the phenomenon of spontaneous appearance of circulation (swirl) in Taylor cones when a parameter (the Reynolds number) exceeds a threshold value, we have considered the axisymmetric motion of a liquid inside the conical domain of Fig. 3. The motion is driven by a stress in the radial direction $\tau_{r^*,\theta}$ acting at the conical surface. The axisymmetric Navier-Stokes equations governing the problem are solved numerically. Since, as in real electrospays, there is no direct mechanism of swirl generation, we are looking for the conditions at which intense swirl motion appears in addition to the meridian motion generated by the forcing stress.

The paper is structured as follows: Equations and boundary conditions for the modeling of the flow inside Taylor cones as well as a brief description of the numerical scheme used to integrate the equations are given in Sec. II. Finally, results are presented and discussed in Sec. III.

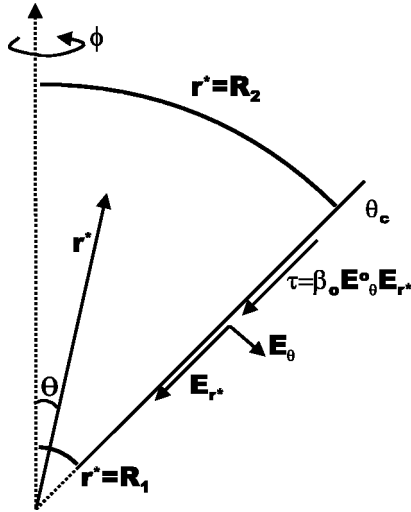


FIG. 3. Sketch of the conical domain considered in the problem.

II. PHYSICAL MODEL

We have considered the motion of a liquid inside the conical domain sketched in Fig. 3,

$$R_1 \leq r^* \leq R_2, \quad 0 \leq \theta \leq \theta_c, \quad (1)$$

R_2 is typically the distance from vertex to needle, and R_1 is small as compared to R_2 . The needle diameter is related to R_2 as $d = 2R_2 \sin \theta_c$, where θ_c is the cone semiangle.

At the conical surface ($\theta = \theta_c$), we assume that there is a tangential stress pointing to the vertex, which drives the liquid motion. This stress depends on the dimensional distance to the vertex r^* as

$$\tau_{r^*\theta}(r^*) = -\text{Re} \frac{\rho \nu^2}{R_2^2} \left(\frac{R_2}{r^*} \right)^l, \quad (2)$$

where ρ is the density of the liquid, ν is the kinematic viscosity, and l is any positive real number. Note that we have excluded the small region near the vertex $0 \leq r^* < R_1$ from the domain since the Navier-Stokes equations in spherical coordinates are singular at the origin; also the driving stress (2) becomes singular at the origin. Note also that the Reynolds number has been defined here from the strength of the driving stress. Therefore, if one introduces arbitrarily a characteristic velocity of the motion defined as

$$V_c = \frac{R_2 \tau_{r^*\theta}(R_2)}{\rho \nu}, \quad (3)$$

the Reynolds number of the motion has the usual form $\text{Re} = V_c R_2 / \nu$.

In real electrosprays, the value of the exponent l in Eq. (2) is close to the value $l = 2.5$ [10]. In fact, the electrical stress is given by $\tau_{r^*\theta} \approx \beta_o E_\theta E_{r^*}$, where the normal component of the electric field is approximately given by Taylor's value [15],

$$E_\theta^o = \left(\frac{\gamma}{\beta_o r^* \tan \theta_c} \right)^{1/2}, \quad (4)$$

and the radial component of the electrical field is almost exclusively due to electrical conduction,

$$E_{r^*} = - \frac{I}{2\pi(1 - \cos \theta_c) K r^{*2}}, \quad (5)$$

where γ is the liquid-gas surface tension, β_o is the permittivity of the vacuum, K is the electrical conductivity of the liquid, and I is the current emitted throughout the jet.

A. Governing equations

For the numerical computation of the axisymmetric motions considered here, it is useful to introduce a stream function-vorticity formulation. Therefore, we define dimensionless axisymmetric meridian stream function Ψ and a circulation Γ such as

$$u_r = \frac{1}{r^2 \sin \theta} \frac{\partial \Psi}{\partial \theta}, \quad u_\theta = - \frac{1}{r \sin \theta} \frac{\partial \Psi}{\partial r}, \quad (6)$$

and

$$u_\phi = \frac{\Gamma}{r \sin \theta}, \quad (7)$$

where u_r , u_θ , and u_ϕ are the radial, polar, and azimuthal components of the dimensionless velocity of the liquid. All variables are dimensionless and R_2 and ν/R_2 have been chosen as scales of length and velocity, respectively. Therefore,

$$\Psi = \bar{\Psi}/\nu \quad \text{and} \quad \Gamma = \bar{\Gamma}/\nu, \quad (8)$$

where $\bar{\Psi}$ and $\bar{\Gamma}$ are dimensional stream function and circulation, respectively. In addition, we define the new variable η (related to the azimuthal vorticity ω_ϕ) in the form

$$\eta = r \sin \theta \omega_\phi = \sin \theta \left(\frac{\partial(r u_\theta)}{\partial r} - \frac{\partial u_r}{\partial \theta} \right), \quad (9)$$

so that, taking into account Eq. (6), Eq. (9) reads

$$\eta = - \frac{\partial^2 \Psi}{\partial r^2} - \frac{1}{r^2} \left(\frac{\partial^2 \Psi}{\partial \theta^2} - \cot \theta \frac{\partial \Psi}{\partial \theta} \right). \quad (10)$$

Two additional equations for Γ and η are obtained from both the azimuthal momentum equation

$$\frac{D\Gamma}{Dt} = \frac{\partial^2 \Gamma}{\partial r^2} + \frac{1}{r^2} \left(\frac{\partial^2 \Gamma}{\partial \theta^2} - \cot \theta \frac{\partial \Gamma}{\partial \theta} \right), \quad (11)$$

and the azimuthal vorticity equation

$$\begin{aligned} \frac{D\eta}{Dt} = & -\frac{2\Gamma}{r^3 \sin \theta} \frac{\partial \Gamma}{\partial \theta} + \frac{2\Gamma \cos \theta}{r^2 \sin^2 \theta} \frac{\partial \Gamma}{\partial r} + \frac{2\eta}{r^3 \sin \theta} \frac{\partial \Psi}{\partial \theta} \\ & - \frac{2\eta \cos \theta}{r^2 \sin^2 \theta} \frac{\partial \Psi}{\partial r} + \frac{\partial^2 \eta}{\partial r^2} + \frac{1}{r^2} \left(\frac{\partial^2 \eta}{\partial \theta^2} - \cot \theta \frac{\partial \eta}{\partial \theta} \right), \end{aligned} \quad (12)$$

where

$$\frac{D}{Dt} = \frac{\partial}{\partial t} - \frac{1}{r^2 \sin \theta} \frac{\partial \Psi}{\partial r} \frac{\partial}{\partial \theta} + \frac{1}{r^2 \sin \theta} \frac{\partial \Psi}{\partial \theta} \frac{\partial}{\partial r} \quad (13)$$

is the total derivative.

B. Initial and boundary conditions

At $t=0$, the liquid is assumed to be at rest, hence

$$\Psi = \Gamma = \eta = 0, \quad (14)$$

at any point inside the considered domain $\delta = R_1/R_2 \leq r \leq 1$, $0 \leq \theta \leq \theta_c$. Alternatively, any steady solution with a Reynolds number close to that of the numerical solution we are looking for may be used as initial condition to start the numerical integration.

In real situations the gas-liquid interface, whose shape results from a balance of the capillary, electrical, and dynamical pressures, does not differ substantially from the conical surface $\theta = \theta_c$. This observed conical symmetry is explained from the fact that the effect of the dynamical pressure is almost negligible as compared to the other two effects (the Taylor solution corresponds to the static case). This quasispherical shape gives strong support to the assumption that indeed the shear stress at the surface of the conical meniscus follows a power law with r as given by Eq. (2).

Therefore, at $\theta = \theta_c$ we have for the driving stress

$$\sigma_{r,\theta}|_{\theta=\theta_c} = \left[\frac{r}{2} \frac{\partial}{\partial r} \left(\frac{u_\theta}{r} \right) + \frac{1}{2r} \frac{\partial u_r}{\partial \theta} \right]_{\theta=\theta_c} = -\text{Re } r^{-1} \quad (15)$$

and

$$\sigma_{\phi\theta}|_{\theta=\theta_c} = \left[\frac{\sin \theta}{2r} \frac{\partial}{\partial \theta} \left(\frac{u_\phi}{\sin \theta} \right) \right]_{\theta=\theta_c} = 0, \quad (16)$$

where σ stands for dimensionless shear stress at the boundaries. Since $u_\theta = 0$ at $\theta = \theta_c$, Eqs. (15) and (16) taking into account Eqs. (9) and (10) become

$$\eta = 2 \text{Re} \sin \theta_c r^{1-l} \quad \text{and} \quad \frac{\partial \Gamma}{\partial \theta} - 2\Gamma \cot \theta_c = 0 \quad \text{at} \quad \theta = \theta_c. \quad (17)$$

The boundaries of the domain in Fig. 3 are assumed to be impermeable, so that

$$\Psi = 0 \quad \text{at} \quad \theta = 0, \theta = \theta_c, r = \delta, \quad \text{and} \quad r = 1. \quad (18)$$

In principle, condition (18) on the spherical surfaces $r = \delta$ and $r = 1$ would have nothing to do with real Taylor cones where there is a net flow rate through it. The azimuthal velocity will increase enormously along the converging streamlines that issue throughout the jet, but circulation will remain almost constant. As shown in the analysis, the amplification (generation) of circulation, which occurs in Taylor cones, is due to bifurcation from a primary meridian recirculating swirl-free flow. In real situations such a flow presents when the injected flow rate is near the minimum one compatible with a stable cone-jet mode configuration. In this case, the velocities due to the electrical stress are much larger than those due to the injected flow rate and most of the liquid recirculates along meridian planes. Since we are interested in the description of the trigger mechanism of such bifurcation, we have not considered the influence of a nonzero, but small, flow rate.

Conditions of regularity and symmetry must be satisfied at the axis, $\theta = 0$,

$$u_\phi = u_\theta = \frac{\partial u_r}{\partial \theta} = 0; \quad (19)$$

the corresponding conditions for Γ and η are

$$\eta = \Gamma = 0 \quad \text{at} \quad \theta = 0. \quad (20)$$

Reliable boundary conditions at the spherical surfaces $r = \delta$ and $r = 1$ cannot be obtained from experimental observations since the measurements of the velocity field inside the electrified meniscus are still lacking. On the other hand, Eq. (11) is linear in Γ , so that some source of angular momentum is needed to have solutions of the axisymmetric Navier-Stokes equations with nonzero circulation. In electrocapillary flows this source could be due to some nonsymmetric conditions of the capillary needle (roughness, skewness, etc). Therefore, to model the influence of small perturbations in the circulation at the upper boundary $r = 1$, we assume

$$\Gamma = \epsilon \sin^2 \theta \quad \text{at} \quad r = 1, \quad (21)$$

where ϵ is a nondimensional constant that is assumed to be very small ($\epsilon \ll 1$). The dependence of Γ on θ in Eq. (21) is just the one to satisfy the conditions for Γ in both the axis and the conical surface. Clearly, the numerical solution will depend on the chosen value of ϵ , so that, for each value of ϵ , one would find different bifurcation diagrams for circulation (one diagram for each value of ϵ); the critical Reynolds number at which bifurcation occurs being a function of ϵ . Nonetheless, if ϵ is small enough, the numerical solution and the critical Reynolds number become independent of ϵ . Note that the limit case $\epsilon = 0$ is different. In this case no bifurcation occurs and only the trivial solution $\Gamma = 0$ exists.

In addition, we suppose that the forcing stress at the conical surface is the only source of azimuthal vorticity in the domain [see first equation in Eq. (17)], so that, we assume

$$\eta = 0 \quad \text{at} \quad r = \delta \quad \text{and} \quad r = 1. \quad (22)$$

Finally, regarding boundary conditions on Γ at $r = \delta$, we arbitrarily assume

$$\frac{d\Gamma}{dr} = 0. \quad (23)$$

As an alternative to condition (23), we have considered that the surface stress in the ϕ direction vanishes at $r = \delta$

$$\sigma_{\phi r} = 0 \quad \text{or, equivalently,} \quad \frac{d\Gamma}{dr} - 2\Gamma = 0. \quad (24)$$

The use of these two alternative boundary conditions allows us to know their influence on the swirl generation process. As shown by the numerical results the swirl generation is independent of using either Eq. (23) or Eq. (24). System of second-order, nonlinear partial differential equations (10)–(12) together with initial and boundary conditions (14), (18), (17), (20), (21), (22), and either (23) or (24) yield the values of Ψ , Γ , and η as functions of the variables r , θ , and t and dimensionless parameters Re , δ , θ_c , l , and ϵ .

C. Numerical procedures

We have used two different numerical schemes to solve Eqs. (10)–(12). The time evolution of the flow inside the domain has been calculated by using an explicit method. Alternatively, a Newton-Raphson scheme have been used to obtain steady state solutions of Eqs. (10)–(12). In the first method, Eqs. (10)–(12) are discretized in space using a second-order central-difference approximation to spatial derivatives; a uniform grid of $M \times N$ nodes in the numerical domain has been considered. A two-step, second-order predictor-corrector scheme has been used to integrate Eqs. (11) and (12) in time. Finally, we have used the matrix diagonalization method [16], whose computational complexity is of the order $NM \min(M, N)$, to solve efficiently the Poisson equation in Eq. (10). Several mesh sizes and different integration time steps depending on both the Reynolds number Re , and the geometrical parameters δ and θ_c have been used to integrate the discretized equations. The main drawback of this method is that the integration time needed to reach a steady state solution from a given initial condition increases with the Reynolds number.

Bifurcation diagrams can be obtained with much less computational effort using a Newton-Raphson scheme to obtain steady solutions. In this second numerical scheme, the resultant equations of removing the time law derivatives in Eqs. (10)–(12) are discretized using second-order central differences. It yields a system of $3M \times N$ nonlinear algebraic equations for the unknown values Γ_k, η_k, Ψ_k in each node $k = (m, n)$, $1 \leq m \leq M, 1 \leq n \leq N$. This nonlinear system can be written as

$$F(\Psi, \Gamma, \eta; \lambda) = 0, \quad (25)$$

where F is the matrix resulting from the discretization procedure and λ represents the characteristic parameter vector of the problem, which in our case contains Re , θ_c , δ , ϵ , and l .

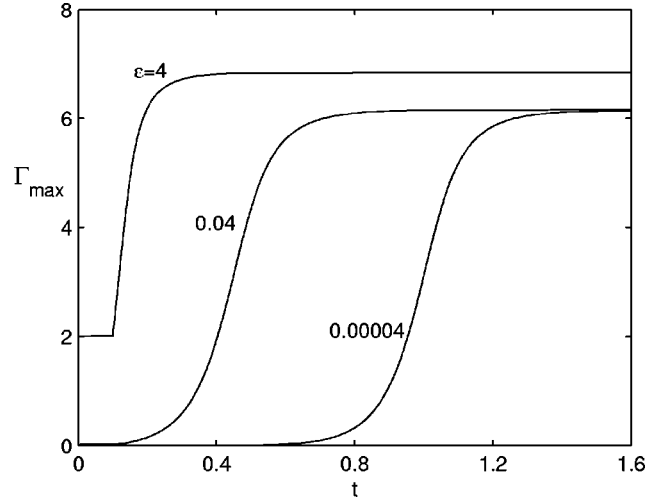


FIG. 4. Time evolution of the maximum circulation in the domain for three different values of ϵ and for $\text{Re} = 8.95$, $\delta = 0.1$, and $\theta_c = 45^\circ$.

We solve the nonlinear system (25) using a standard Newton-Raphson procedure from an initial guess

$$DF(\Psi^i, \Gamma^i, \eta^i; \lambda)(\delta\Psi, \delta\Gamma, \delta\eta) = -F(\Psi^i, \Gamma^i, \eta^i; \lambda), \quad (26)$$

$$\Psi^{i+1} = \Psi^i + \delta\Psi, \quad \Gamma^{i+1} = \Gamma^i + \delta\Gamma, \quad \eta^{i+1} = \eta^i + \delta\eta. \quad (27)$$

Finally, we have used and standard iterative GMRES solver (Slatec package from ITL) to calculate efficiently the inverse sparse Jacobian matrix DF .

III. DISCUSSION OF RESULTS

A. Bifurcation diagrams

The time evolution of the maximum value of circulation Γ_{max} in the conical domain is shown in Fig. 4. It has been calculated numerically for $\text{Re} = 8.95$, $\delta = 0.1$, $\theta_c = 45^\circ$, $l = 2.5$, and three different values of ϵ ($\epsilon = 4 \times 10^{-5}$, $\epsilon = 0.04$, and $\epsilon = 4$). We found that if the Reynolds number is greater than a threshold value Re_c (critical value), the steady state value of the maximum circulation experiences an enormous amplification with respect to the value of the seeded perturbation ϵ (see the cases $\epsilon = 4 \times 10^{-5}$ and $\epsilon = 0.04$ in Fig. 4), while no amplification occurs for values of the Reynolds number smaller than the critical value. As expected, the numerical solution depends on the value of ϵ ; the steady state value Γ_{max}^s being different in the case $\epsilon = 4$ than in the other two cases. Note, however, that for values of ϵ sufficiently small, the differences between the values of the steady state become practically indistinguishable from each other (see the cases $\epsilon = 0.04$ and $\epsilon = 4 \times 10^{-5}$).

The *independence* of the steady solution on the seeded perturbation ϵ , for ϵ small, is due to the enormous amplification undergone by the maximum circulation during the transient process. In the case, $\epsilon = 0.4 \times 10^{-5}$, Γ_{max}^s is about one hundred and fifty thousand times larger than the imposed

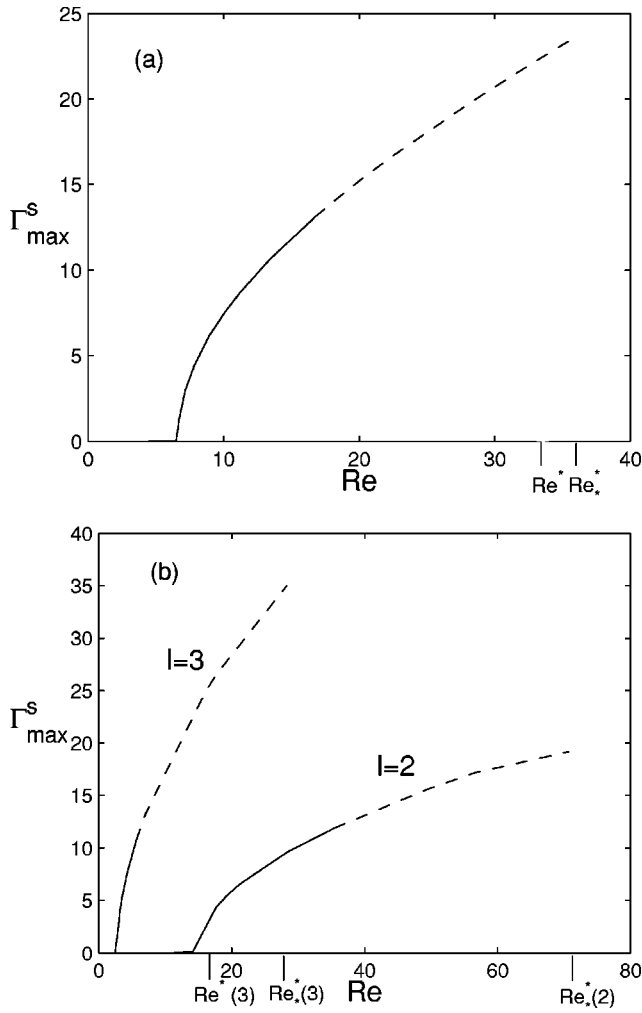


FIG. 5. Bifurcation diagram of the steady state value of the maximum circulation in the domain, Γ_{max}^s , as a function of the Reynolds number for $l=2.5$, $\delta=0.1$, and $\theta_c=45^\circ$. The dashed part of the curve corresponds to flows with vortex breakdown. Values of both Re^* and Re_c^* are indicated on the x axis. (b) Bifurcation diagrams of the steady state value of the maximum circulation in the domain, Γ_{max}^s , as a function of the Reynolds number for $\delta=0.1$, $\theta_c=45^\circ$, and two values of l . The dashed part of the curves corresponds to flows with vortex breakdown. Values of both Re^* and Re_c^* are indicated on the x axis.

value of the perturbation; this figure is one thousand times less in the other case, $\epsilon=0.04$. Note that, for a given value of the Reynolds number and as long as ϵ is small, the same steady flow can be reached through unsteady processes that start from different initial conditions; the larger the value of ϵ the shorter the required time to reach the steady state value.

In Fig. 5(a), we have plotted the bifurcation diagram of Γ_{max}^s (solid and dashed parts of the curves) as a function of the Reynolds number for $\delta=0.1$, $\theta_c=45^\circ$, and $l=2.5$; the cases $l=2$ and $l=3$ are plotted in Fig. 5(b). It can be observed in both figures that for values of the Reynolds number smaller than a critical one, $Re_c(l)$, which depends on l , the flow is meridional, swirl-free, and stable under symmetric small perturbations while it bifurcates to a swirling flow for values of the Reynolds number larger than $Re_c(l)$. As shown

in Figs. 5(a) and 5(b), the value of the critical Reynolds number decreases when l increases; $Re_c \approx 10.2$, $Re_c \approx 6$, and $Re_c \approx 2.8$ for $l=2$, $l=2.5$, and $l=3$, respectively. This behavior lies on the fact that for given values of both the Reynolds number and the geometrical parameters, the driving stress (15) and consequently the induced velocities increase with l . Therefore, the larger the value of l the smaller the Reynolds number at which convection becomes important to shoot up the instability mechanism.

It should be pointed out that the bifurcation diagrams can be also obtained by shedding an initial circulation (small perturbation) in the whole domain instead of forcing with a small perturbation at $r=1$. We found that if the Reynolds number is smaller than the critical one, $Re < Re_c$, the initial perturbation in the domain is damping down and a solution with $\Gamma^s=0$ is obtained. On the contrary, for Reynolds numbers larger than the critical, the flow evolves towards a $\Gamma^s \neq 0$ solution. Numerical calculations show that circulation remains zero at any time if both the forcing perturbation at boundary $r=1$ is zero ($\epsilon=0$), and no circulation perturbation is shed in the whole domain. This is due to the fact that if Γ is zero every where at a given time t_o , the numerical evaluation of each term in Eq. (11) leads identically to zero at any time $t > t_o$. That is, the truncation and round-off errors are zero in the numerical integration of Eq. (11) if $\Gamma=0$ in the domain and its boundary at the initial time.

Let us finally point out that the effect of nonsymmetric perturbations on the flow, which has not been considered here, they could be analyzed either by numerical simulation or by a linear analysis of the stability of the symmetric solutions under small nonsymmetric perturbations. Nonetheless, both studies are beyond the scope of this work.

B. Instability mechanism

The instability mechanism may be explained bearing the circulation equation in mind

$$\frac{d\Gamma}{dt} = \nabla^2 \Gamma - \mathbf{v} \cdot \nabla \Gamma. \tag{28}$$

At sufficiently small Reynolds numbers, convection of circulation Γ is negligible. Circulation is transported by diffusion from the boundary $r=1$ and its value inside the domain grows with time until a steady state is reached. At any time, the maximum circulation is located at $r=1$ and its value is of the order of ϵ . No circulation amplification takes place.

If the effect of viscosity decreases (higher values of the Reynolds number) Γ is transported by both convection and diffusion. The converging meridian motion transports circulation from boundary $r=1$ towards $r=\delta$. Appreciable circulation gradients in the θ direction are generated near the axis by this meridian motion. Thus, circulation is transported by diffusion from the axis towards the conical surface from where it is convected back towards the axis. This circulation pumping, due to diffusion, is essential to close the feedback loop that shoots the circulation amplification mechanism for

Reynolds numbers larger than the critical value. The steady state value is reached by saturation.

Note, finally, that the instability mechanism here described has nothing to do with the well-known increase of swirl velocity due to the vortex stretching mechanism. In that case, circulation (angular momentum) remains constant along the fluid trajectories (high Reynolds number flows). On the contrary, in this case, circulation is amplified by a mechanism that combines convection of circulation towards the axis along the outermost streamlines and feedback diffusion transport from the axis towards the outer streamlines. As a result, the swirl-less, recirculating, meridian flow bifurcates to a swirling flow, for Reynolds numbers greater than a critical one. Diffusion transport is therefore the ultimate mechanism responsible for the change of circulation experienced along the streamlines.

C. Circulation quenching at increasing Reynolds numbers

Beyond Re_c , swirling flows are found numerically as far as the value of the Reynolds number is less than a value called hereafter $Re_*^*(l)$. For values of the Reynolds number greater than Re_*^* , swirling regimes are not found numerically, so that, we conclude that the only stable solutions for $Re > Re_*^*$ are those with $\Gamma = 0$. As shown in Fig. 5, the value of $\Gamma_{max}^s(Re)$ grows monotonically with the Reynolds number in the interval $Re_c < Re < Re_*^*(l)$. The values of Re_*^* obtained numerically for the cases $l=2, 2.5$, and 3 are, respectively, $71, 36$, and 28 .

Let us now compare the bifurcation diagram found in conical self-similar flows with that given in Fig. 5(b) for $l=2$. In conical self-similar flows, there exists bifurcated swirling flows in the interval $Re_c < Re < \infty$. On the contrary, we found numerically that the existence of swirling flows is restricted to the interval $Re_c < Re < Re_*^*$. In both the cases, the value of the maximum circulation inside the domain increases monotonically when the Reynolds number increases. Also, we found numerically a critical Reynolds number for the case $l=2$ that is slightly larger than the one reported in the self-similar case [12].

The reasons for this apparent discrepancies between numerical and self-similar solutions are discussed in the following. The thickness of the axis zone where diffusion is important decreases when the Reynolds number increases. In fact, this thickness is of the order of $\nu/V_c \sim R_2/Re$. Therefore, the circulation pumping by diffusion from the axis could not reach the conical surface if the thickness of the diffusion zone is smaller than the minimum distance between the axis and the conical surface, which is of the order of R_1 . In that case, which occurs for Reynolds numbers larger than a certain value Re_*^* , circulation cannot be pumped by diffusion from the axis towards the cone surface. Then, the maximum circulation is of the order of ϵ and no circulation amplification takes place. In fact, we found that for a given value of δ there is a value of Reynolds number $Re_*^*(\delta)$, which is a function of δ , such as no circulation amplification exists for Reynolds numbers larger than Re_*^* . Only non-swirling meridian flows present for $Re > Re_*^*$ since the circu-

lation pumped by diffusion cannot reach the conical surface because the axis to conical surface distance is for these Reynolds numbers larger than the corresponding viscous penetration length.

Numerical results show that the parametric range of the Reynolds numbers, $Re_c \leq Re \leq Re_*^*$, for which swirling flows present, widens out when lesser values of R_1 , with R_2 fixed, are considered. In particular, for the case $l=2$ and R_1 decreasing, the value of the critical Reynolds number Re_c found numerically approaches to the critical value of the self-similar analysis while Re_*^* increases monotonously as R_1 goes to zero. Note that to have an efficient pumping of circulation from the axis towards the outer boundary, the characteristic distance R_1 at the domain must be smaller or comparable to the viscous penetration, or equivalently, the Reynolds number of the flow should be smaller than Re_*^* . In conical self-similar flows Re_*^* becomes infinite [12], since the ratio between convection and diffusion is independent of the distance r from the origin and beyond the critical Reynolds number Re_c circulation increases monotonically with Re .

A peculiarity of the flows with $l > 2.4$ is the existence of two metastable regimes in the interval $Re_* < Re < Re_*^*$, [see Figs. 5(a) and 5(b)]. In that interval of Reynolds numbers, one of the two metastable regimes corresponds to the $\Gamma = 0$ regime and the other to the bifurcated swirling one, while only swirling flows are found to exist in the interval $Re_c \leq Re \leq Re_*^*$. Re^* corresponds to the maximum value of the Reynolds number for which a solution with amplification $\Gamma \neq 0$ is obtained when the numerical integration is started from the rest. The $\Gamma = 0$ regime is unstable under symmetric small perturbations in the interval $Re_c \leq Re \leq Re_*^*$, while it is not in $Re^* \leq Re \leq Re_*^*$. The initial condition at which the numerical integration is started determines which of the two metastable regimes is finally reached. For example, if Re_1 is a value of the Reynolds number lying in the interval $Re_* \leq Re_1 \leq Re_*^*$, the numerical solution with $\Gamma \neq 0$ corresponding to that value of the Reynolds number may be obtained in the following way. First, one must choose a value of the Reynolds number Re_2 lying in the interval $Re_c \leq Re_2 \leq Re_*$ and calculate numerically the solution for $Re = Re_2$. This solution must be used as initial condition of the numerical integration to find the required solution for $Re = Re_1$. Alternatively, if a Newton-Raphson scheme is used, the solution corresponding to $Re = Re_2$ must be used as an initial guess. This is the easier and faster method to find the nonzero Γ branch of the interval $Re_* \leq Re_1 \leq Re_*^*$ since the final numerical solution is obtained in a few iterations. For $l=2.5$ and $l=3$, we have found numerically $Re^* \approx 33$ and $Re^* \approx 16$, respectively. The width of the region where the two metastable regimes exist, $Re_*^* - Re_*$ increases with l and approaches to zero for $l=2.4$.

D. Vortex breakdown

The existence of internal flow separation at the axis, or vortex breakdown, is another interesting feature of these swirling flows with forcing at the surface. Vortex breakdown

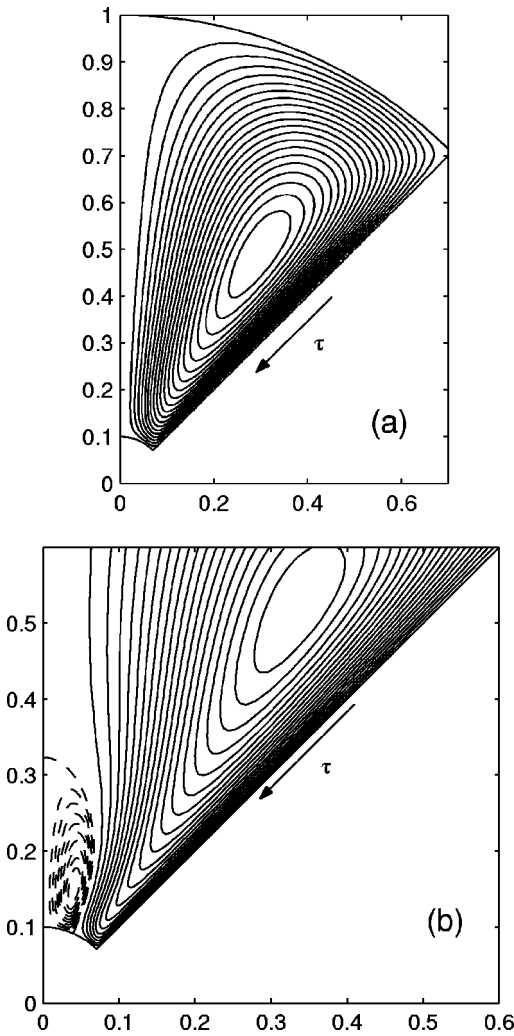


FIG. 6. Steady state one-cell meridional streamlines for the case $Re=5.6$, $l=3$, $\delta=0.1$, and $\theta_c=45^\circ$. (b) Steady state double-cell meridional streamlines for the case $Re=25$, $l=3$, $\delta=0.1$, and $\theta_c=45^\circ$.

takes place when the azimuthal to radial velocity ratio reaches a threshold value. It entails a strong modification of the meridional flow, which changes abruptly from a single-cell structure like the one shown in Fig. 6(a) to a double cell with a counter-recirculating bubble near the axis, see Fig. 6(b). There is a stagnation point at the axis, which separates the axis zone where velocities are negative (towards the vertex) from that where velocities are positive. The meridional back flow near the axis (towards the vertex along the axis) is a consequence of the low pressure induced there by the effect of the centrifugal forces. The plot of the meridional streamlines in Fig. 6(b) indicate that, in the outer cell, velocities are large near the conical surface and in the jetlike flow leaving the $r=\delta$ region, while in the inner cell the fluid is almost stagnant. Steady state swirling flows with double-cell structure are represented on the dashed part of the bifurcated swirling curve in Fig. 5. Note that in this case, vortex breakdown does not prevent the growing of the maximum circulation of the flow when the Reynolds number is increased. In fact, the jetlike flow, which develops along the axis in single cell,

moves inside the domain when vortex breakdown takes place. The distance between the region where circulation is accumulated and the outer surface is less in the case of a double-cell flow than in the single-cell one. Therefore, in spite of the occurrence of vortex breakdown, the pumping of circulation by diffusion still works efficiently and stronger values of circulation are generated in the outer cell. Clearly, for Reynolds numbers greater than Re_*^* , the transport of circulation by diffusion is unable to reach the outer surface and only swirl-free flows are found to exist since the self-rotation mechanism does not work efficiently any more.

It should be finally pointed out that in electrocapillary flows, vortex breakdown takes place at Reynolds numbers of order of unity, which are much lower than those of the vortex breakdown experiments described in the literature. Let us now comment some of the differences between the vortex breakdown occurring at very high Reynolds numbers (treated in previous works) and that at Reynolds number of order of unity characteristic of the flows considered here. At high Reynolds number swirling flows, vortex breakdown appears as a catastrophic event. The flow pattern changes drastically when the swirl parameter (usually a characteristic swirl to axial velocity ratio) is slightly increased beyond a critical value, with the sudden appearance of a large counter-recirculating bubble in the meridional flow. A concrete, clear-cut example illustrating the mathematical scenario of vortex breakdown in flows at high Reynolds was provided by the near-axis analysis of nearly inviscid vortices [18]. These authors found that vortex breakdown appears when the singularities at the axis that often appears in axisymmetric inviscid swirling flows cannot be regularized through thin viscous cores. In those cases, the near-axis viscous vortex equations governing the viscous core of the vortex fail to have a solution. This behavior shows that viscosity plays an important role in the existence of these nearly inviscid vortices and supports the theory proposed by Hall [17] on vortex breakdown as analogy to boundary layer separation.

That is not, clearly, the situation in flows at moderately Reynolds numbers where viscosity is not restricted to very thin regions of the flow. In our case, for example, a small bubble first appears when the Reynolds number slightly overpasses the critical value (the flow separates at some point at the axis with immediate reattachment) and the bubble size increases gradually with increasing the Reynolds number. Clearly, in the cases of spontaneous generation of circulation (self-rotation) the double cell disappears for Reynolds numbers larger than Re_*^* for which circulation is almost zero. In flows with forced circulation as those generated by a rotating disk (see for example Refs. [19] and [20] among others), this nonabrupt kind of vortex breakdown has been also observed. An incipient small bubble presents at a Reynolds number slightly greater than the critical value (of the order of 1000) and whose size grows when the Reynolds number increases.

E. Influence of the cone angle

The influence of the cone angle θ_c on the bifurcation diagram is shown in Fig. 7, where we have plotted values of

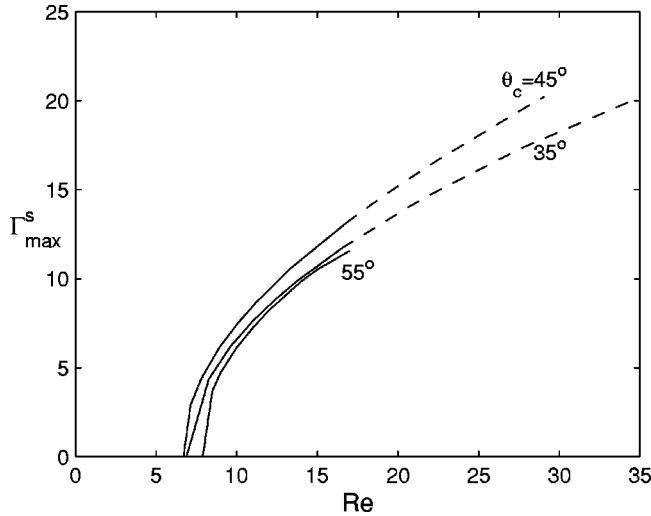


FIG. 7. Influence of the cone angle on the bifurcation diagrams for $\delta=0.1$ and $l=2.5$. The dashed part of the curves corresponds to flows with vortex breakdown.

Γ_{max}^s as a function of the Reynolds number for three different values of the cone angle. Note that there exists a value of the cone angle θ_c close to 45° for which the circulation amplification is maximum. Note that larger values of θ_c put limits to the pumping mechanism of circulation while lower values of θ_c lead to lower values of the driving stress, for a given value of the Reynolds number [see the first condition in Ref. [13]]. Therefore, there exists a value of θ_c , which is found to be close to 45° for which the self-rotation process results to be more efficient. It should be pointed out that for $\theta_c=55^\circ$, the strength of the circulation is lower than in the two other cases and the azimuthal to radial velocity ratio is lower than the threshold value required for the existence of vortex breakdown. Numerical results also show that there is no amplification of circulation if θ_c is larger than $\pi/2$. This result can be explained from condition in Eq. (16) or equivalently the second condition in Eq. (17), which establishes the absence of any forcing in the azimuthal direction acting at the cone surface. This condition that plays a key role in the accumulation process of circulation at the corner (δ, θ_c) of the domain, shows that $d\Gamma/d\theta|_{\theta=\theta_c}$ is positive (negative) for values of the cone angle θ_c smaller (larger) than $\pi/2$. Since the extreme of Γ must be located at the boundaries, the maximum of Γ would be located at the corner (δ, θ_c) only if $\theta_c < \pi/2$. Otherwise, the maximum must be located at the boundary $r=1$ and, therefore, there is no amplification in the value of circulation inside the domain. For conical flows, Ref. [12] reported the same result when the cone angle is larger than $\pi/2$.

Let us now comment the influence of using condition (24) instead of Eq. (23) on the process of generating circulation. When condition (24) is used, the maximum value of the circulation is not longer reached at the corner (δ, θ_c) but at some point (r_1, θ_c) , $\delta < r_1 < 1$. In that case, boundary $r=\delta$ behaves as a sink of circulation, $d\Gamma/dr \neq 0$ at $r=\delta$ when condition (24) (zero stress in the ϕ direction) is used, and therefore the values reached by circulation are much smaller

than those in the case of zero circulation flux condition (or *adiabatic* boundary) $d\Gamma/dr=0$.

Although the detailed experimental results of the velocity field inside Taylor cones are not still available, it may be finally instructive, however, to compare typical values of the azimuthal velocity obtained numerically with those estimated from experimental measurements in electrospays [8]. In the electrospaying of heptane ($\rho=684 \text{ kg/m}^3$ and $\nu=5.7 \times 10^{-7} \text{ m}^2/\text{s}$ at room conditions), values of the Reynolds number close to 10 and azimuthal velocities of a few centimeters per second has been reported. For $\text{Re}=10$, $l=2.5$, and $\theta_c=35$ (the value of θ_c closer to the experimental meniscus semiangle, see Fig. 4) one obtains from Fig. 7(a) value of the dimensionless circulation $\Gamma_{max}^s \approx 6$. Therefore, from Eq. (8), the dimensional circulation is

$$\bar{\Gamma}_{max} = \nu \Gamma_{max}^s \approx 6 \nu, \quad (29)$$

and for a capillary needle of $R_2=10^{-3} \text{ m}$, the typical value of the maximum azimuthal velocity is

$$v_\phi^* \sim \frac{\bar{\Gamma}_{max}}{\delta R_2} \approx 3 \text{ cm/s}, \quad (30)$$

which is the value of the typical velocity reported in Ref. [9].

IV. SUMMARY

Recirculating meridian fluid flows inside Taylor cones are observed in the electrospaying of liquids with sufficiently large values of both the viscosity and the electrical conductivity. In these motions, which are mainly driven by the electrical stresses acting at the cone surface, the liquid flows towards the cone vertex, along the generatrix, and away from it along the axis. In addition to the recirculating meridian motion, an intense swirl is also observed when liquids with smaller values of viscosity and electrical conductivity are electrospayed. This transition from a nonswirling recirculating meridian motion to a swirling one takes place when the characteristic Reynolds number of the flow is larger than a critical value.

To model this phenomenon, we have considered the flow driven by a tangential stress at the generatrix of the conical domain sketched in Fig. 3. A small region containing the cone vertex has been excluded from the domain to avoid singularities in the computational process. The parameters that govern the problem are the Reynolds number of the motion, the geometrical parameters δ and θ_c , and a real number l that characterizes the r dependence of the driven stress. An unsteady, axisymmetric Navier-Stokes numerical code is used to solve this problem. Therefore, the influence of nonsymmetric perturbations on the generation of swirl has not been considered in this analysis.

Numerical results show that a nonswirling meridian flow bifurcates to a swirling one for values of the Reynolds number larger than a critical one, Re_c . Values of Re_c are calculated for several values of l , θ_c , and δ . The amplification process of circulation is due to an advection-diffusion transport mechanism of circulation. Small perturbations in circu-

lation existing in the boundary $r=1$ are convected by the meridian recirculatory motion; towards the vertex along the conical surface, and away of it along the axis. Large gradients of circulation in the θ direction are generated in the near-axis region from where circulation is transported towards the conical surface by diffusion. A steady state value is reached when both diffusion and convection are balanced. For Reynolds numbers higher than the critical one, $Re_c(l)$, which depends on l , this convection-diffusion transport feedback loop is very efficient and large values of circulation are reached. The value of the steady state circulation is a growing function of the Reynolds number of the flow.

There exists a value of the Reynolds number Re_*^* such as swirling flows are numerically found for values of the Reynolds number in between of the interval $Re_c < Re \leq Re_*^*$, while only swirl-less flows are found for $Re > Re_*^*$. Re_*^* depends on both the exponent l and the geometrical parameter δ . The nonexistence of swirling flows beyond Re_*^* is due to a given value of δ , the viscous penetration length becomes smaller than the minimum separation distance between the axis and the conical surface and circulation cannot be pumped up to the conical surface by diffusion. Therefore, no amplification of circulation takes place for Reynolds numbers larger than Re_*^* . Numerical results show that the interval $Re_c < Re \leq Re_*^*$ becomes wider when δ decreases with R_2 fixed (Re_c decreases while Re_*^* increases). In particular, for the case $l=2$, the value of Re_c found numerically decreases and approaches to the critical value found in the self-similar analysis when δ decreases with R_2 fixed while Re_*^* increases monotonously.

Bifurcation diagrams with $l > 2.4$ are slightly different to those already described with $l \leq 2.4$. For $l > 2.4$, we found the existence of two kind of flows, with zero and nonzero circulation, which are stable in the interval of Reynolds numbers $Re_*^* \leq Re \leq Re_*^*$, while only swirling flows are found in

the interval $Re_c \leq Re \leq Re_*^*$. The initial conditions at which the numerical integration is started determine which of the two metastable regimes is finally reached. The width of the interval $Re_*^* \leq Re \leq Re_*^*$ widens out with l and goes to zero as l goes to 2.4.

The existence of vortex breakdown is also found numerically when the strength of the swirling-to-meridian motion reaches a threshold value. Flows with vortex breakdown correspond to the dashed part of the bifurcation curves in Fig. 5. The meridian flow is strongly affected by the occurrence of vortex breakdown. The structure of the meridian flow is of the one-cell type in the absence of vortex breakdown; the fluid moves towards the vertex along the conical surface and away from it along the axis. This flow structure changes abruptly to one of the double-cell type when vortex breakdown occurs. In this case, an inner counter-recirculating bubble, where circulation is almost zero and the fluid is almost stagnant, coexists with an outer recirculating cell with nonzero circulation. A dividing streamline that meets the axis in a stagnation point separates the two cells.

The influence of the cone angle θ_c on the generation of circulation has been also studied. We have found that the mechanism of circulation amplification is more efficient for a value of θ_c that is close to 45° .

It should be pointed out finally that the instability mechanism of swirl amplification here described could also appear in other converging flows generated by body forces (natural convection, electrical forces, etc.).

ACKNOWLEDGMENTS

This work was partially supported by the Dirección General de Enseñanza Superior of Spain, through Grant No. BFM2000-0528. The authors thank Dr. J. M. Gordillo, Professor Fernández de la Mora, and Dr. V. Shtern for their valuable comments.

-
- [1] T.B. Jones, *Nature (London)* **389**, 854 (1997).
 - [2] A. Ogawa, *Vortex Flows* (CRC Press, Boca Raton, FL, 1993).
 - [3] M. Kawakuko, Y. Tsuchia, M. Sugaya, and K. Matsumura, *Phys. Lett.* **68A**, 65 (1978).
 - [4] V. Shtern and F. Hussain, *Annu. Rev. Fluid Mech.* **31**, 537 (1999).
 - [5] R. Fernández-Feria and E. Sanmiguel-Rojas, *Phys. Fluids* **12**, 3082 (2000).
 - [6] K.E. Torrance, *J. Fluid Mech.* **95**, 477 (1979).
 - [7] M. Funakoshi and S. Inoue, *J. Fluid Mech.* **192**, 219 (1988).
 - [8] V. Bojarevics, J.A. Freiberger, E.I. Shilova, and E.V. Shcherbinin, *Electrically Induced Vortical Flows* (Kluwer Academic, Dordrecht, The Netherlands, 1989), pp. 136.
 - [9] A. Barrero, A.M. Gañán-Calvo, J. Dávila, A. Palacio, and E. Gómez-Gonzalez, *Phys. Rev. E* **58**, 6 (1998).
 - [10] A.M. Gañán-Calvo, J. Dávila, and A. Barrero, *J. Aerosol Sci.* **28**, 249 (1997).
 - [11] A. Barrero, A.M. Gañán-Calvo, J. Dávila, A. Palacio, and E. Gómez-Gonzalez, *J. Electrost.* **47**, 13 (1999).
 - [12] V. Shtern and A. Barrero, *J. Fluid Mech.* **300**, 169 (1995).
 - [13] V. Shtern and A. Barrero, *Phys. Rev. E* **52**, 627 (1995).
 - [14] R. Fernández-Feria, J. Fernández de la Mora, M. Pérez-Saborid, and A. Barrero, *Quarterly J. Mech. Appl. Math.* **52**, 1 (1999).
 - [15] G.I. Taylor, *Proc. R. Soc. London, Ser. A* **280**, 383 (1964).
 - [16] R.E. Lynch, J.R. Rice, and D.H. Thomas, *Numer. Math.* **6**, 185 (1964).
 - [17] M.G. Hall, *Annu. Rev. Fluid Mech.* **4**, 195 (1972).
 - [18] R. Fernández-Feria, J. Fernández de la Mora, and A. Barrero, *J. Fluid Mech.* **305**, 77 (1995).
 - [19] J.M. Lopez, *J. Fluid Mech.* **221**, 533 (1990).
 - [20] A. Spohn, M. Mory, and E.J. Hopfinger, *J. Fluid Mech.* **370**, 73 (1998).